

Enhanced target normal sheath acceleration using colliding laser pulses

J. Ferri,^{1,*} E. Siminos,² and T. Fülöp¹

¹*Department of Physics, Chalmers University of Technology, 41296 Gothenburg, Sweden*

²*Department of Physics, Gothenburg University, 41296 Gothenburg, Sweden*

(Dated: January 27, 2023)

We show that a strong enhancement of proton acceleration can be achieved with two intense laser-pulses of equal energy incoming on a solid target with opposite incidence angles. Through the use of two-dimensional Particle-In-Cell simulations, we find that the multi-pulse interaction leads to a standing wave pattern at the front side of the target, with an enhanced electric field and a substantial modification of the hot electron generation process. This in turn leads to significant improvement of the proton spectra, with an almost doubling of the accelerated proton energy. The proposed scheme is robust with respect to incidence angles for the laser pulses, providing flexibility to the scheme, which should facilitate its experimental implementation.

Proton acceleration due to the interaction of an ultraintense laser pulse with a thin solid target has been widely studied in the past two decades [1, 2], bringing the field closer to applications, such as medical treatment with proton therapy [3, 4], probing of electric fields [5, 6], isochoric heating for high energy-density physics [7] or triggering fast ignition in inertial confinement fusion [8]. Although many different acceleration mechanisms were suggested, target normal sheath acceleration (TNSA) [9–12] has been the most investigated method, thanks to a relatively simple experimental implementation and the moderate laser-intensity it requires. However, even with the continuous increase in the available laser power, the limited scaling of the maximum energy of the accelerated protons with the laser energy (which in general is, $E_{max} \propto I_0^\alpha$, with $\alpha < 1$ depending on the laser pulse duration [13–15]) constitutes a major drawback for many interesting applications.

Recent experiments proposed a way to improve the performance of the TNSA scheme by splitting the main laser pulse in two less-energetic pulses, incident on the target within a short time delay [16–19]. Previous theoretical work suggested that such a multiple-pulse scheme could be used to produce mono-energetic features in the proton spectrum [20]. Later it was also shown experimentally that it could lead to an enhancement of the maximum proton energy [16, 17], and that high laser-to-proton energy conversion efficiency could be reached [18]. However, the physical mechanism explaining these results relies on a judicious balance between plasma expansion on the front side and on the rear side. As a consequence, these experiments require an accurate control of both the time delay and the energy splitting between the two pulses, leading to a narrow range of parameters and a quite limited energy enhancement. Additionally, in a recent experiment using an equal splitting of the laser energy into two femtosecond laser pulses, no enhancement of the proton energy could be obtained, even with a precise scanning of the time delay [19].

In this Letter, we describe a modified TNSA scheme which consists in the splitting of a laser pulse in two

pulses of equal energy which are incident on the thin solid target simultaneously, but with different angles of incidence. Based on two-dimensional (2D) simulations with the EPOCH Particle-In-Cell (PIC) code [21], we show that the interaction in the resulting standing wave leads to an increase in the peak value of the electric fields and substantial enhancement of the hot electron generation process at a constant laser energy. This in turn leads to a strong increase in the proton energy (from 8.5 to 14 MeV with a 45° angle and a 0.8 J laser) and proton number with realistic laser parameters. Furthermore, we show that these conclusions remain valid for a large range of incidence angles for the laser pulses, including asymmetric configurations.

To illustrate the scheme, an initial 0.8 J laser pulse is splitted in two sub-pulses of 0.4 J. We consider Gaussian

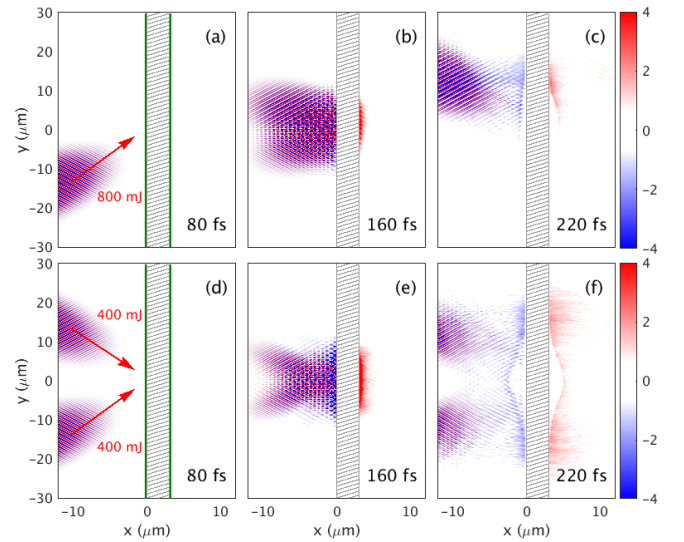


FIG. 1. Map of the longitudinal electric field E_x (TV/m^{-1}) at different times in the reference case (a-c) and the two-pulse case (d-f). The position of the Al target is indicated by the dashed gray lines, and the thin proton layers are shown in green in (a) and (d). The incidence angle is $\phi = 45^\circ$.

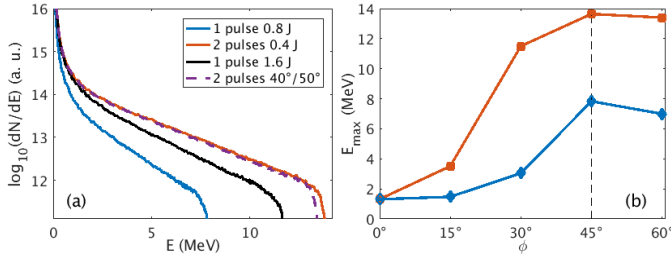


FIG. 2. (a) Proton spectra after 700 fs in the reference case (blue), the two-pulse case (red) and cases with one 1.6 J laser pulse (black) and with two 0.4 J laser pulses but slightly asymmetric incidence angle ($\phi_1 = 40^\circ$ and $\phi_2 = -50^\circ$, dashed purple). (b) Dependence of the maximum proton energy as a function of the incidence angle. For the two-pulse case, the angles are ϕ and $-\phi$. The black dashed lines indicate $\phi = 45^\circ$ on which we mainly focus our analysis.

temporal and spatial profiles for the laser pulses, and a duration $\tau_0 = 38$ fs. These two p -polarized laser pulses are incident on a solid Aluminium (Al) target simultaneously and on the same $5 \mu\text{m}$ spot (corresponding to an intensity $I_0 = 5 \times 10^{19} \text{W}/\text{cm}^2$), but with opposite incidence angle ϕ and $-\phi$ with respect to the target normal in the x, y plane. In the following, the case with one pulse containing the total 0.8 J energy will be referred to as the reference case, in contrast with the two-pulse case. We performed 2D-simulations of these cases with the EPOCH PIC code, using a $44 \times 80 \mu\text{m}^2$ box with a 10 nm resolution, and 50 particles per cell for the electron and ion species. The proton species are assumed to originate from hydrogen-containing contaminants at the surface of the target, and are simulated with 20 nm-thick layers on the front and rear sides of the target, using 1000 particles per cell. The target is assumed to be fully ionized, with initial density $n_i = 50n_c$ for the Al^{13+} ions and $n_e = 13n_i$ for the electrons, with n_c the critical density, and the physical ion-to-electron mass ratio $m_i/m_e = 1836 \times 27$ is used. The scheme is illustrated with snapshots of the E_x longitudinal electric field at different simulation times shown in Fig. 1. The overall laser-matter interaction seems to be similar in both cases at first sight, but note that the two-pulse case leads to a more symmetric mechanism for the generation of the rear-field. Furthermore, an enhancement of the rear field can be seen in the beginning of the interaction (compare Figs. 1(b) and 1(e)).

In Fig. 2(a), we show the proton spectra at the end of the simulation ($t = 700$ fs), in the reference case, the two-pulse case and a case with a pulse with double the energy for an incidence angle $\phi = 45^\circ$. Clearly, the two-pulse scheme leads to a strong increase in the proton energy, with maximum energy \mathcal{E}_{max} increasing from 7.8 MeV to 13.7 MeV when compared with the reference case, i.e. an increase of approximately 80%. Even compared with a case containing twice the total energy, i.e. 1.6 J, in a

single laser pulse, there is a $\sim 20\%$ improvement in the two-pulse case, see the black curve in Fig. 2(a). Moreover, when integrating the spectra, the number of protons above 1 MeV is multiplied by a factor of > 5 in the two-pulse case.

The flexibility of our scheme with respect to the incidence angle is explored in Fig. 2(b), in which the maximum proton energies for the reference and the two-pulse cases are shown for a wide range of incidence angles. In the reference case, a clear peak of the proton energy is observed at 45° , corresponding to the maximum efficiency of the vacuum heating for these angles [22]. In the single-pulse case, the TNSA mechanism is quickly degraded with decreasing angles and is inefficient for small incidence angles. In contrast, in the two-pulse case, the mechanism is sustained for a wider range of angles, with small variation of \mathcal{E}_{max} for ϕ in the range 30° – 60° . As a consequence, the proton energy enhancement is more pronounced for angles of incidence different than the optimal 45° , almost reaching 300% for $\phi = 30^\circ$.

In this paper we mainly explore a symmetric double-pulse case, but the scheme can be extended to asymmetric incidence angles. The practical advantage with the asymmetry is that the reflected laser pulses will not aim straight back for the optics, and therefore the experimental implementation of the scheme will be easier. In Fig. 2(a), we show a proton spectrum corresponding to a two-pulse asymmetric case, with $\phi_1 = 40^\circ$ and $\phi_2 = -50^\circ$. Introducing this asymmetry keeps the results largely unchanged, with the maximum proton energy degraded by a mere 3%. This indicates that the main effect can be detected even in an experiment with e.g. a tilted target in the direction orthogonal to the propagation plane of the laser pulses.

To understand the difference in the acceleration mechanism between the single and multiple-pulse cases we need to study the differences in the electromagnetic field configurations close to the target surface and the ways in which these affect absorption. In our simulations, we observe two different types of electron populations: most of the electrons stay in the first wavelength of the standing wave in front of the target, meaning that they are accelerated through the vacuum heating mechanism [23, 24] over a single wavelength of the electromagnetic wave. By contrast, a small proportion of the population is ejected further away and is usually re-injected in the target with slightly higher average momentum. For this population, additional stochastic heating is present, but this effect remains marginal in both cases (as also noted in Ref. [25]).

For simplicity, and since we are mostly interested in qualitatively understanding how the two cases differ in terms of the vacuum heating mechanism, we consider the target as a perfect conductor, i.e. the laser pulses are perfectly reflected on the surface of the target. One could then describe the incoming and reflected fields as an effective multi-pulse configuration in the half-space

in front of the target. Letting N be the number of effective pulses, we have $N = 2$ pulses of intensity I_0 in the reference case and $N = 4$ pulses of intensity $I_0/2$ in the two-pulse case [cf. Fig. 3(a) and 3(d)]. The key benefit of a multi-pulse system is that the field amplitude scales as \sqrt{N} , as observed in Ref. 26, where three-dimensional solutions for the field of focused pulses were obtained. For the sake of simplicity, we here consider the case of N plane waves, with vector-potentials given by $A_n = A_0 \sqrt{N/2} \cos(\omega_0 t - k_0 \cos(\phi_n)x - k_0 \sin(\phi_n)y)$, where ϕ_n is the angle of incidence for the n^{th} pulse, $\omega_0 = 2\pi c/\lambda_0$ and $k_0 = \omega_0/c$, with c the speed of light. For p -polarized waves, the electric field E_x in front of the target can then be written:

$$E_{x,2} = -2 \sin \phi E_0 \sin(t - y \sin \phi) \cos(x \cos \phi), \quad (1)$$

$$E_{x,4} = 2\sqrt{2} E_0 \sin \phi \cos t \sin(y \sin \phi) \cos(x \cos \phi), \quad (2)$$

where time has been normalized on ω_0^{-1} and coordinates on k_0^{-1} , the incident angles are assumed to be symmetric with respect to the x axis and $E_{x,N}$ denotes the field in the case of N effective pulses. The peak field is increased by $\sqrt{2}$ in the two-pulse case ($N = 4$) compared to the reference case ($N = 2$). It can also be seen that in the two-pulse case a standing wave is obtained in front of the target, where the fields are $2\pi/\omega_0$ periodic in time. These fields are shown in Figs. 3(b) and 3(e), and can be compared with the fields obtained from the simulations, at the time of interaction of the peak of the laser pulse with the target (and at the peak value of the fields for the two-pulse case) [Figs. 3(c) and 3(f)]. Note, that the analytical and simulation fields are similar close to the focal spot, particularly in the two-pulse case. In the reference case, the field symmetry is slightly changed by the modification of the reflected pulse (partial absorption and high-harmonic generation).

Although the vacuum heating mechanism has been the subject of intense study at increasing levels of sophistication [22, 27–29], here we are merely interested in developing a qualitative understanding of the differences between the single- and double-pulse cases. We will thus only consider the simple “capacitor” model originally formulated by Brunel [23]. For a perfect conductor, it yields for the average power absorbed per laser cycle,

$$P_a \propto E_d \left[(1 + e^2 E_d^2 / m_e^2 c^2 \omega_0^2)^{1/2} - 1 \right],$$

where the capacitor field E_d is related to the driving longitudinal field by $E_d = 2E_0 \sin \phi$ for the single pulse case and by $E_d = 2\sqrt{2}E_0 \sin \phi$ for the two-pulse case. In general, the absorbed power would be expected to scale as $P_a \propto N E_0^2$ in a configuration with N effective pulses. However, one has to note that for focused pulses the field enhancement and the associated increase in absorption is *localized* close to the focus. Since introducing more than

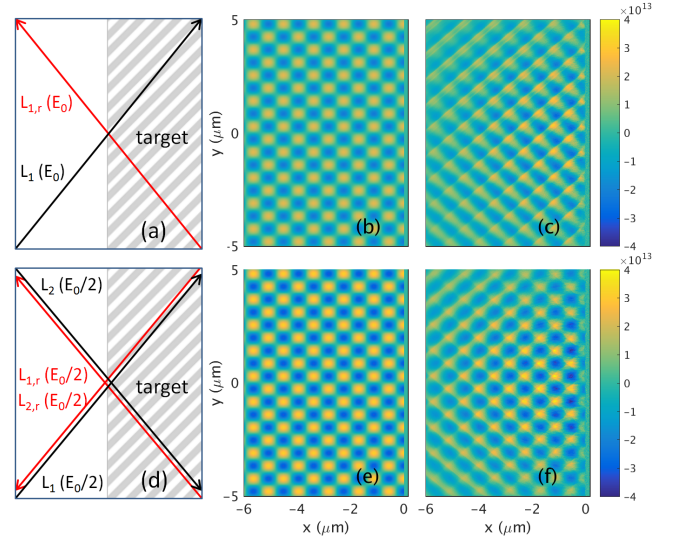


FIG. 3. Scheme of the multi-pulse interaction for the reference case (a) and the two-pulse case (d). Analytical longitudinal electric field E_x (V/m) obtained from equations (1) [resp. (2)] (b) [resp. (e)]. Snapshot of the longitudinal electric field E_x (V/m) in front of the target from the reference simulation (c) and the two-pulse simulation (f) after 155 fs (corresponding to the peak interaction).

$N = 4$ effective pulses would complicate the experimental implementation of the scheme, we will not consider this generalization here.

The field enhancement in the focus of a N -pulse system is however not sufficient to completely explain the difference between the two schemes. The capacitor model has been derived by assuming a longitudinal standing wave field in front of the target, while it neglects the effect of the $\mathbf{v} \times \mathbf{B}$ force on the electrons. As already noted in Ref. [23] these approximations are only valid in a two-pulse but not in a single-pulse case. This becomes clear if we take a closer look at the change of relative phase between the E_x and B_z fields. As noted in Ref. 24, the positions of the maxima of the $|E_x|$ field on the target surface coincide with nodes for the B_z field in the two-pulse case, as shown in Fig. 4(a). Therefore, in the two-pulse case, the electron motion is mainly determined by the quiver motion in the E_x field as the $\mathbf{v} \times \mathbf{B}$ force is negligible, and one can see that the electrons reaching high energy originate from the region on the target surface corresponding to the maxima of $|E_x|$. However, in the single-pulse case B_z is not zero at these positions [see Fig. 4(b)], so the $\mathbf{v} \times \mathbf{B}$ force acts on the electrons, and inhibits the force due to E_x [27].

The dependence of the proton energy on the incidence angle, shown in Fig. 2(b), can also be understood considering the relative effect of the $E_x \propto E_0 \sin \phi$ and the $v_y \times B_z \propto E_0 B_0 \cos \phi$, where $B_0 \sim E_0/c$ is the single pulse peak magnetic field. For the single-pulse case, E_x then decreases with smaller ϕ while $v_y \times B$ increases,

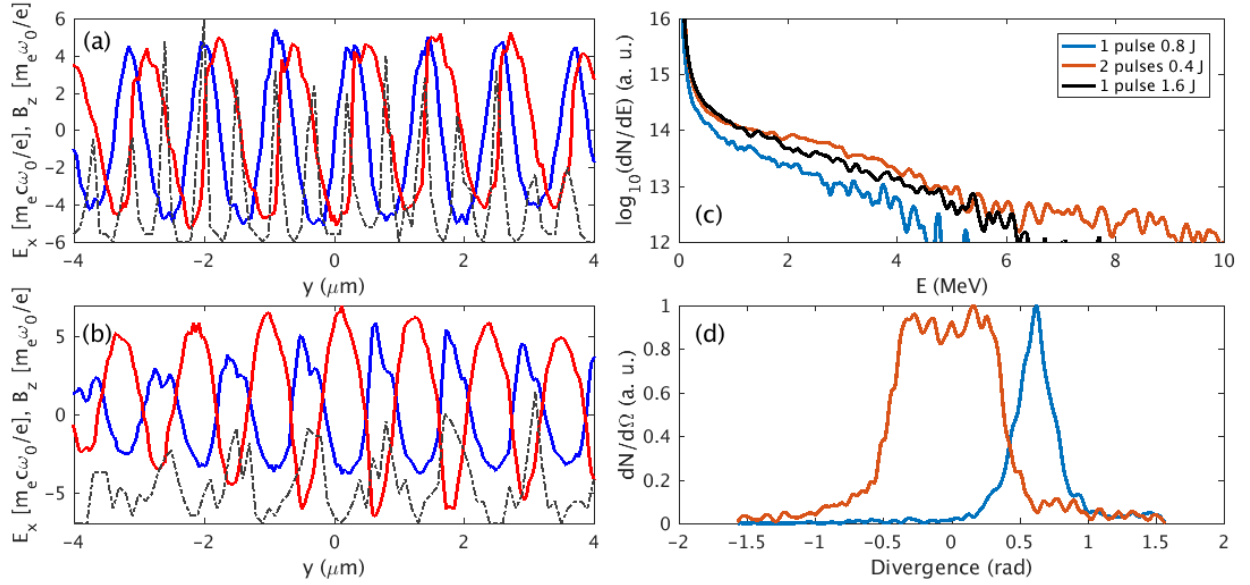


FIG. 4. (a) (resp (b)) E_x (blue) and B_z (red) fields on the target surface at $t = 150$ fs in the two-pulse case (resp. reference case). The dashed black lines indicate the distribution of the initial y position on the target surface for the electrons reaching 400 keV during the simulation. For the reference case, this distribution is plotted in the frame moving with a $c \sin \phi$ velocity along y to take into account the drifting of the fields. (c) Electron spectra and (d) divergence of the hot electron beam after 160 fs (interaction of the peak of the laser pulse with the target) for the reference case (blue), the two-pulse case (red) and a case with only one pulse but twice the total energy (black).

quickly deteriorating the hot electron generation. This is not the case in the two-pulse setup, for which B_z is zero at the maxima of $|E_x|$.

The above effects explain that, compared to the single-pulse case, the two-pulse configuration leads to an increased number and energy of the vacuum-accelerated electrons. This is confirmed in the electron spectra presented in Fig. 4(c), taken from the simulation during the interaction of the peak of the laser pulse with the Al target, where we can see that larger number and more energetic hot electrons are generated in the two-pulse case. We also plot the electron spectra obtained with a single laser pulse with twice the energy (1.6 J, black). In this configuration, the peak field is the same as in the two-pulse case with 0.8 J of total energy, but the temperature of the spectra is still inferior, showing the importance of the two-pulse geometry where the $\mathbf{v} \times \mathbf{B}$ force does not cancel E_x . The higher hot electron energy density will in turn impact the electrostatic fields generated on the rear of the target [which was shown in Fig. 1(e)], for the benefit of the TNSA process. The increase in the proton energies are indeed coherent with the standard estimate for the rear sheath field $E_{x, \text{sheath}} \propto \sqrt{n_H T_H}$ [30], with n_H and T_H the hot electron density and temperature obtained from Fig. 4(c).

We also note a change in the divergence of the electron beam, shown in Fig. 4(d). In the single-pulse scheme, the electrons are preferentially accelerated in the direction of the incoming laser pulse, with a peak of the distribution

at $\sim 35^\circ$. As expected in the symmetric two-pulse mechanism, the hot electron divergence is centered along the x -axis. In this case, however, the divergence of the electron beam is increased, so the rear TNSA fields should decrease faster with increasing thickness of the target.

As the efficiency of the scheme relies on the vacuum acceleration mechanism, taking into account the effect of a preplasma is expected to affect the performance of the scheme. Simulations indeed show that with a $2 \mu\text{m}$ -long preplasma with an exponential profile ranging from $0.01n_c$ to $100n_c$, the increase in the proton energy is still above 40%, but this increase becomes lower as the preplasma length increases. Therefore, experimental implementation of this scheme requires ultra-high intensity contrast, which can be achieved e.g. with a double plasma mirror [31, 32]. It is also important to note that, provided that the time difference is much shorter than the pulse duration, the efficiency of the two-pulse scheme does not depend on the relative phase between the two laser pulses, as the standing wave pattern is determined by the reflection conditions, and this fact was verified in simulations.

In conclusion, we have proposed a modification of the TNSA scheme aiming to enhance the proton energy at a constant laser energy. By splitting a main laser pulse into two laser pulses, simultaneously incident on a target at different angles, we can access a different energy repartition of the electromagnetic fields on the front side of the target, which in turn can generate a higher number

of hotter electrons. This leads to a significant enhancement of the proton energy ($\sim 80\%$ for a constant laser energy), and the number of protons (increase by a factor > 5). The robustness of this scheme, in particular with respect to the incident angles, makes it a strong case for future experiments, as setups allowing for spatial and temporal separation of a laser pulse have already been implemented [33, 34]. This scheme then potentially allows for higher performance of the TNSA mechanism than what can be obtained through temporal pulse shaping, and could possibly be further optimized by splitting the laser pulse into more numerous sub-pulses.

The authors would like to acknowledge fruitful discussions with L Gremillet, I Thiele, J Martins, L Yi and the PLIONA team. This work was supported by the Knut and Alice Wallenberg Foundation and by the Swedish Research Council, Grant No. 2016-05012. The simulations were performed on resources at Chalmers Centre for Computational Science and Engineering (C3SE) provided by the Swedish National Infrastructure for Computing (SNIC, Grants SNIC 2017/1-484, SNIC 2017/1-393, SNIC 2018/1-43).

* julienf@chalmers.se

- [1] H. Daido, M. Nishiuchi, and A. S. Pirozhkov, Rep. Prog. Phys. **75**, 056401 (2012).
- [2] A. Macchi, M. Borghesi, and M. Passoni, Rev. Mod. Phys. **85**, 751 (2013).
- [3] S. V. Bulanov and V. S. Khoroshkov, Plasma Phys. Rep. **28**, 453 (2002).
- [4] S. Bulanov, T. Esirkepov, V. Khoroshkov, A. Kuznetsov, and F. Pegoraro, Physics Letters A **299**, 240 (2002).
- [5] M. Borghesi, S. Kar, L. Romagnani, T. Toncian, P. Antici, P. Audebert, E. Brambrink, F. Ceccherini, C. Cecchetti, J. Fuchs, M. Galimberti, L. Gizzi, T. Gris-mayer, T. Lyseikina, R. Jung, A. Macchi, P. Mora, J. Osterholtz, A. Schiavi, and O. Willi, Laser and Particle Beams **25**, 161 (2007).
- [6] L. Romagnani, M. Borghesi, C. Cecchetti, S. Kar, P. Antici, P. Audebert, S. Bandhoupadajay, F. Ceccherini, T. Cowan, J. Fuchs, M. Galimberti, L. Gizzi, T. Gris-mayer, R. Heathcote, R. Jung, T. Liseykina, A. Macchi, P. Mora, D. Neely, M. Notley, J. Osterholtz, C. Pipahl, G. Pretzler, A. Schiavi, G. Schurtz, T. Toncian, P. Wilson, and O. Willi, Laser and Particle Beams **26**, 241 (2008).
- [7] P. K. Patel, A. MacKinnon, M. H. Key, T. E. Cowan, M. E. Ford, M. Allen, D. F. Price, H. Ruhl, P. T. Springer, and R. Stephens, Phys. Rev. Lett. **91**, 125004 (2003).
- [8] M. Roth, T. E. Cowan, M. H. Key, S. P. Hatchett, C. Brown, W. Fountain, J. Johnson, D. M. Pennington, R. A. Snavely, S. C. Wilks, K. Yasuike, H. Ruhl, F. Pegoraro, S. V. Bulanov, E. M. Campbell, M. D. Perry, and H. Powell, Phys. Rev. Lett. **86**, 436 (2001).
- [9] S. C. Wilks, A. B. Langdon, T. E. Cowan, M. Roth, M. Singh, S. Hatchett, M. H. Key, D. Pennington, A. MacKinnon, and R. A. Snavely, Phys. Plasmas **8**, 542 (2001).
- [10] E. L. Clark, K. Krushelnick, M. Zepf, F. N. Beg, M. Tatarakis, A. Machacek, M. I. K. Santala, I. Watts, P. A. Norreys, and A. E. Dangor, Phys. Rev. Lett. **85**, 1654 (2000).
- [11] R. A. Snavely, M. H. Key, S. P. Hatchett, T. E. Cowan, M. Roth, T. W. Phillips, M. A. Stoyer, E. A. Henry, T. C. Sangster, M. S. Singh, S. C. Wilks, A. MacKinnon, A. Offenberger, D. M. Pennington, K. Yasuike, A. B. Langdon, B. F. Lasinski, J. Johnson, M. D. Perry, and E. M. Campbell, Phys. Rev. Lett. **85**, 2945 (2000).
- [12] A. Maksimchuk, S. Gu, K. Flippo, D. Umstadter, and V. Y. Bychenkov, Phys. Rev. Lett. **84**, 4108 (2000).
- [13] J. Fuchs, P. Antici, E. d'Humières, E. Lefebvre, M. Borghesi, E. Brambrink, C. Cecchetti, M. Kaluza, V. Malka, M. Manclossi, S. Meyroneinc, P. Mora, J. Schreiber, T. Toncian, H. Pèpin, and P. Audebert, Nature physics **2**, 48 (2006).
- [14] L. Robson, P. T. Simpson, R. J. Clarke, K. W. D. Ledingham, F. Lindau, O. Lundh, T. McCanny, P. Mora, D. Neely, C.-G. Wahlstrom, M. Zepf, and P. McKenna, Nature Phys. **3**, 58 (2007).
- [15] K. Zeil, S. D. Kraft, S. Bock, M. Bussmann, T. E. Cowan, T. Kluge, J. Metzkes, T. Richter, R. Sauerbrey, and U. Schramm, New J. Phys. **12**, 045015 (2010).
- [16] K. Markey, P. McKenna, C. M. Brenner, D. C. Carroll, M. M. Günther, K. Harres, S. Kar, K. Lancaster, F. Nürnberg, M. N. Quinn, A. P. L. Robinson, M. Roth, M. Zepf, and D. Neely, Phys. Rev. Lett. **105**, 195008 (2010).
- [17] G. Scott, J. Green, V. Bagnoud, C. Brabetz, C. Brenner, D. Carroll, D. MacLellan, A. Robinson, M. Roth, C. Spindloe, F. Wagner, B. Zielbauer, P. McKenna, and D. Neely, Appl. Phys. Lett. **101**, 024101 (2012).
- [18] C. M. Brenner, A. P. L. Robinson, K. Markey, R. H. H. Scott, R. J. Gray, M. Rosinski, O. Deppert, J. Badziak, D. Batani, J. R. Davies, S. M. Hassan, K. L. Lancaster, K. Li, I. O. Musgrave, P. A. Norreys, J. Pasley, M. Roth, H.-P. Schlenvoigt, C. Spindloe, M. Tatarakis, T. Winstone, J. Wolowski, D. Wyatt, P. McKenna, and D. Neely, Applied Physics Letters **104**, 081123 (2014).
- [19] J. Ferri, L. Senje, M. Dalui, K. Svensson, B. Aurand, M. Hansson, A. Persson, O. Lundh, C.-G. Wahlström, L. Gremillet, E. Siminos, T. C. DuBois, L. Yi, J. Martins, and T. Fülöp, Physics of Plasmas **25**, 043115 (2018).
- [20] A. P. L. Robinson, D. Neely, P. McKenna, and R. G. Evans, Plasma Physics and Controlled Fusion **49**, 373 (2007).
- [21] T. D. Arber, K. Bennett, C. S. Brady, A. Lawrence-Douglas, M. G. Ramsay, N. J. Sircombe, P. Gillies, R. G. Evans, H. Schmitz, A. R. Bell, and C. P. Ridgers, Plasma Physics and Controlled Fusion **57**, 1 (2015).
- [22] P. Gibbon and A. R. Bell, Phys. Rev. Lett. **68**, 1535 (1992).
- [23] F. Brunel, Phys. Rev. Lett. **59**, 52 (1987).
- [24] F. Brunel, The Physics of Fluids **31**, 2714 (1988).
- [25] A. Yogo, S. V. Bulanov, M. Mori, K. Ogura, T. Z. Esirkepov, A. S. Pirozhkov, M. Kanasaki, H. Sakaki, Y. Fukuda, P. R. Bolton, H. Nishimura, and K. Kondo, Plasma Physics and Controlled Fusion **58**, 025003 (2016).
- [26] S. S. Bulanov, V. D. Mur, N. B. Narozhny, J. Nees, and V. S. Popov, Phys. Rev. Lett. **104**, 220404 (2010).

- [27] J. P. Geindre, P. Audebert, and R. S. Marjoribanks, [Phys. Rev. Lett. **97**, 085001 \(2006\)](#).
- [28] A. Debayle, J. Sanz, L. Gremillet, and K. Mima, [Phys. Plasmas **20**, 053107 \(2013\)](#).
- [29] P. Mulser, S. M. Weng, and T. Liseykina, [Physics of Plasmas **19**, 043301 \(2012\)](#).
- [30] P. Mora, [Phys. Rev. Lett. **90**, 185002 \(2003\)](#).
- [31] H. C. Kapteyn, M. M. Murnane, A. Szoke, and R. W. Falcone, [Optics letters **16**, 490 \(1991\)](#).
- [32] G. Doumy, F. Quéré, O. Gobert, M. Perdrix, P. Martin, P. Audebert, J. C. Gauthier, J.-P. Geindre, and T. Wittmann, [Phys. Rev. E **69**, 026402 \(2004\)](#).
- [33] B. Aurand, M. Hansson, L. Senje, K. Svensson, A. Persson, D. Neely, O. Lundh, and C.-G. Wahlström, [Laser and Particle Beams **33**, 59 \(2015\)](#).
- [34] B. Aurand, L. Senje, K. Svensson, M. Hansson, A. Higginson, A. Gonoskov, M. Marklund, A. Persson, O. Lundh, D. Neely, P. McKenna, and C.-G. Wahlstrom, [Phys. Plasmas **23**, 023113 \(2016\)](#).